Direct Measurement of Absorption-Induced Wavefront Distortion in Cavities with High Optical Power

Aidan F. Brooks,[1,2] David Hosken,[1] Jesper Munch,[1] Peter J. Veitch,[1] Zewu Yan,[3] Chunnong Zhao,[3] Yaohui Fan,[3] Ju Li,[3] David Blair,[3] Phil Willems[2] and Bram Slagmolen[4]

[1]*Department of Physics, The University of Adelaide,*
Adelaide, South Australia 5005, Australia

[2]*LIGO Laboratory, California Institute of Technology*
1200 East California Boulevard, Pasadena CA, 91125, USA

[3]*School of Physics, The University of Western Australia*
35 Stirling Highway, Nedlands, Western Australia 6009, Australia

[4]*Centre for Gravitational Physics, The Australian National University*
Canberra, ACT, 0200 Australia

Wavefront distortion due to absorption in the substrates and coatings of mirrors in advanced gravitational wave interferometers has the potential to seriously compromise the operation and sensitivity of these interferometers. We report the first direct measurement of wavefront distortion, recorded using an ultra-high sensitivity Hartmann wavefront sensor and a dedicated test facility. © 2008 Optical Society of America

OCIS codes: 280.4788, 350.6830, 120.2230.

1. Introduction

The first generation of long baseline interferometric detectors of gravitational waves, including the LIGO [1], VIRGO [2], GEO600 [3] and TAMA300 [4] detectors, have begun astrophysical observations. The initial LIGO interferometers have now reached their design sensitivity over a broad range of frequencies [5] and extended observations, in collaboration with other detectors, are being used to place significant upper limits on the amplitude of the gravitational waves produced by a variety of predicted astrophysical sources [6–9]. While the detection of gravitational waves from these sources using the initial detectors is possible, it is

unlikely for observation times of about 1 year. Thus, higher sensitivity advanced detectors, including Advanced LIGO [10] and LCGT [11], which will have detection rates that are a factor of 1000 higher than for initial LIGO, are planned. Successful development of these advanced detectors will herald the birth of observational gravitational wave astronomy and will open a revolutionary new window to the universe.

The sensitivity of initial detectors at frequencies above about 200 Hz is limited by photon shot noise. Thus, in advanced detectors, the power stored in the interferometer will be increased, for example by a factor of about 20 in Advanced LIGO. However, optical absorption in the substrates and coatings of the interferometer mirrors and beam-splitter will result in wavefront distortion due to thermo-optic, elasto-optic and thermo-elastic effects [12–14]. This distortion could seriously compromise the operation of the interferometer and will degrade the sensitivity of the detector [14]. Various compensation techniques have therefore been proposed, including minimization of the absorption and controlled heating of the intra-cavity optics by radiative heating rings or by CO_2 laser beams [14].

To enable adequate compensation, however, wavefront sensors that have high sensitivity, good long-term stability and suitable spatial resolution, and that can be incorporated into the complex gravitational wave interferometers (GWI) are required. For example, the Advanced LIGO design specifies a wavefront sensor that has an RMS wavefront sagitta sensitivity better than 1.35 nm (equivalent to approximately $\lambda/600$ at a measurement wavelength of 800 nm) over a 230 mm aperture and a spatial resolution of less than 10 mm over this aperture [15]. We have recently reported development of an ultra-sensitive Hartmann wavefront sensor that can measure wavefront changes with a precision of $\lambda/15,500$ and an accuracy of $\lambda/3,300$ at a measurement wavelength of 800 nm [16]. Furthermore, it has a suitable spatial resolution and is simple to optimize.

Here we show that this sensor has a sensitivity that satisfies the Advanced LIGO specification when used to measure absorption-induced wavefront distortion in a mirror suspended in a large vacuum system. More importantly, perhaps, we report the first direct measurement of absorption-induced wavefront distortion in an optical cavity that has high stored optical power. The accuracy of the measured wavefront distortion is confirmed by comparing the calculated effect of the distortion on the cavity mode size with an independent measurement of that size. Additionally, the accuracy is demonstrated by comparing the measured distortion with a finite element model of the distortion based on the observed cavity power.

2.   Measurement system

The measurements reported here were recorded at the High Optical Power Test Facility (HOPTF) [17], a collaborative project between the Australian Consortium for Interferometric Astronomy (ACIGA) and the LIGO project, located near Gingin in Western Australia. The
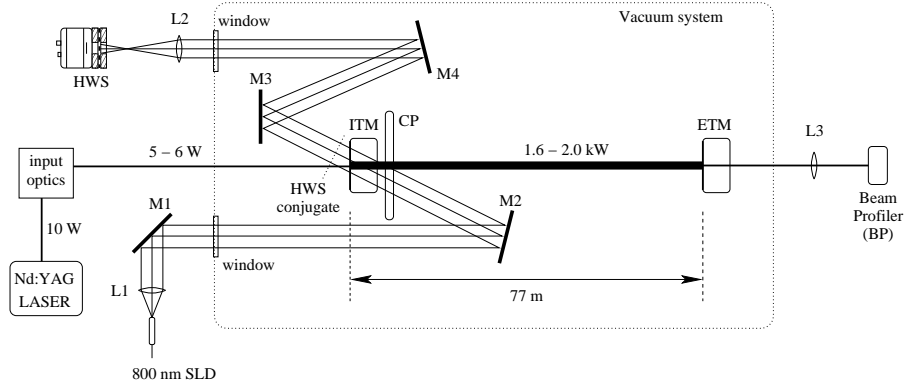
Fig. 1. Schematic layout of the measurement system. The ITM and ETM form a high finesse Fabry-Perot cavity in which up to 2.0 kW can be stored. Absorption by the ITM and CP substrate results in wavefront distortion that is measured using an off-axis Hartmann wavefront sensor (HWS)

aim of this facility is to investigate high-power operation of suspended optical cavities. The initial test Fabry-Perot cavity, shown in Fig. 1, consists of a flat sapphire input-coupling mirror, or input test mass (ITM), that is reversed so that the substrate is within the cavity (to increase the power absorbed in the substrate) and a highly reflecting concave mirror, or end test mass (ETM). The cavity also contains a fused silica compensation plate (CP) that was used previously to demonstrate wavefront correction by conductive heating of the plate [18]. The optical and physical properties of the mirrors and CP are listed in Table 1. The cavity has a finesse of about 1400 and a nominal cold-cavity waist of 8.7 ± 0.3 mm.

The input laser beam is produced by a single-frequency 10 W Nd:YAG laser [20]. After frequency stabilization and mode-cleaning using a monolithic reference cavity, a maximum power of approximately 6 W is incident on the Fabry-Perot cavity, yielding a maximum stored power of about 2.0 kW. The mode matching between the input laser beam and the cavity mode is not completely stable and the intra-cavity power fluctuates. A small part of the cavity mode leaks through the ETM, enabling the stored power and mode size to be monitored using a commercial beam profiler (BP).

In this configuration, thermal lenses will form in the ITM and CP in accordance with the theory of Hello and Vinet [12]. The thermal lenses exist as volumetric distortions (thermo-refractive and elasto-optic) and as surface deformations (thermo-elastic) of the optics and induce wavefront distortion in the resonant cavity mode. Due to the vastly different thermal diffusivities of sapphire and fused silica, the thermal lenses will form at significantly different rates. This effect has previously been observed indirectly by monitoring the behaviour of the cavity mode [18].

	ITM	ETM	CP
Material	Sapphire	Sapphire	Fused Silica
Diameter	100 mm	150 mm	160 mm
Thickness	46 mm	80 mm	17 mm
Radius of curvature	flat	720 ± 100 m	flat
Transmittance	1840 ± 100 ppm	20 ppm	n/a
AR reflectance	30 ± 20 ppm	12 ± 10 ppm	100 ppm
Thermal conductivity	33 W m^{-1} K^{-1}	33 W m^{-1} K^{-1}	1.38 W m^{-1} K^{-1}
Absorption	≈ 50 ppm/cm	n/a	≈ 5.5 ppm
Thermo-optic coefficient (dn/dT)	13×10^{-6} K^{-1}	13×10^{-6} K^{-1}	10×10^{-6} K^{-1}

Table 1. Physical parameters of the HOPTF Fabry-Perot cavity optics [19]. The absorption of the ITM is dominated by substrate absorption and is the value for the sapphire from which it was fabricated. The absorption for the CP was estimated from the ratio of the measured distortion due to the ITM and CP.

The induced wavefront distortion is measured using a Hartmann wavefront sensor (HWS) [16] in an off-axis configuration to enable the distortion induced by each optic to be measured separately. A fibre-coupled superluminescent diode that has a peak wavelength of 800 nm and a coherence length of order 10 μm is used as the light source for the HWS. The output of the fibre is collimated using lens L1 to form an 80 mm diameter Hartmann beam which enters and exits the vacuum system through optical-quality windows and is transmitted through the ITM and CP at an angle of approximately 10°. In this configuration the centers of the ITM and CP are separated horizontally by approximately 23 mm when viewed at the off-axis angle. Lens L2 images the output face of the ITM onto the Hartmann plate with a demagnification factor of approximately 7. All beams outside the vacuum system are enclosed in beam tubes to reduce the effect of air currents.

The Hartmann plate consists of a thin brass disc into which a hexagonally-close-packed array of about 1000 holes (150 μm diameter, 430 μm pitch) has been drilled. It is bolted to the front of an 11-bit dynamic range, 1024×1024 pixel CCD camera. The distance between the plate and the active surface of the CCD, the lever-arm, is 10.43 ± 0.02 mm [16]. The plate divides an incident wavefront into a series of rays that propagate normal to the local wavefront and form spots on the CCD.

Absorption-induced wavefront distortion is measured by recording reference spot positions before power is stored in the cavity and then recording the spot positions for the distorted

wavefront. Spot centroids are calculated using a weighted centroiding algorithm [21]

$$\{x_c, y_c\} = \left\{ \frac{\sum_{ij} i\, I_{ij}^2}{\sum_{ij} I_{ij}^2}, \frac{\sum_{ij} j\, I_{ij}^2}{\sum_{ij} I_{ij}^2} \right\} \tag{1}$$

where the summation is only over pixels in the region of a spot and where I_{ij} is the pixel digital number of the ij-th pixel which depends on the intensity illuminating that pixel. Thus it is important that the beam illuminating the Hartmann plate and the CCD does not contain fluctuating interference fringes as they would degrade the accuracy of the centroiding. The short coherence length of the light source used was critical in removing these fringes and reducing the noise in the centroids.

Dividing the changes in the centroids by the lever arm length yields the change in local gradient of the wavefront due to the absorption, which can be plotted as a discrete gradient field. A map of the wavefront distortion is calculated by numerically integrating the gradient field.

3. Measurements

The in-situ sensitivity of the HWS was determined by recording 20 contiguous Hartmann images at 53 Hz with no power stored in the cavity, and calculating the wavefront map using centroids averaged over the first and last groups of 10 images, giving an RMS wavefront error of $\lambda/730$. This sensitivity is substantially worse than the estimated shot-noise-limited sensitivity of about $\lambda/3000$ [16], probably due to residual air currents in the much larger volume of air in the beam path. Nevertheless, it still satisfies the Advanced LIGO specification.

A low noise *reference* Hartmann measurement was made by recording and averaging 300 individual measurements of the spot positions over a period of approximately 6 seconds. The 1064 nm laser beam was then coupled into the cavity and the absorption-induced wavefront distortion was monitored by continuously recording spot positions at 53 Hz for 300s. These spot positions were averaged over 10 contiguous measurements, yielding gradient fields at 5.3 Hz. The BP recorded the profile of the cavity eigenmode at the ETM at 10 Hz. The zero moment of the profile was used to monitor the power stored in the mode.

This procedure was repeated many times. The power measured by the BP, as a function of time, for two different instances is plotted in Fig. 2, where $t = 0\,\text{s}$ is the time when the laser was first frequency-locked to the cavity-mode. The upper curve (Test I) shows a measurement of the power with relatively unstable mode-matching and the lower (Test II) shows a measurement of the power with relatively stable mode-matching. The corresponding beam size measurements are shown in Fig. 3. The unstable case (Test I) was chosen for the analysis reported here as it provides a more compelling demonstration of the robustness of the HWS.
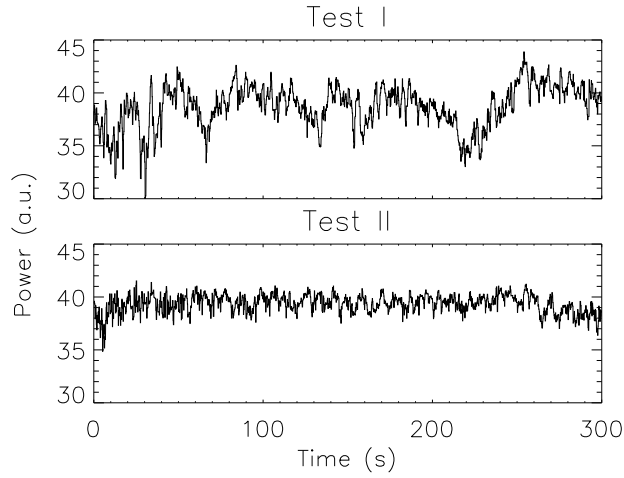
Fig. 2. Time dependence of the power transmitted through the ETM, as recorded by the beam profiler, for relatively unstable mode-matching (Test I) and relatively stable mode-matching (Test II).
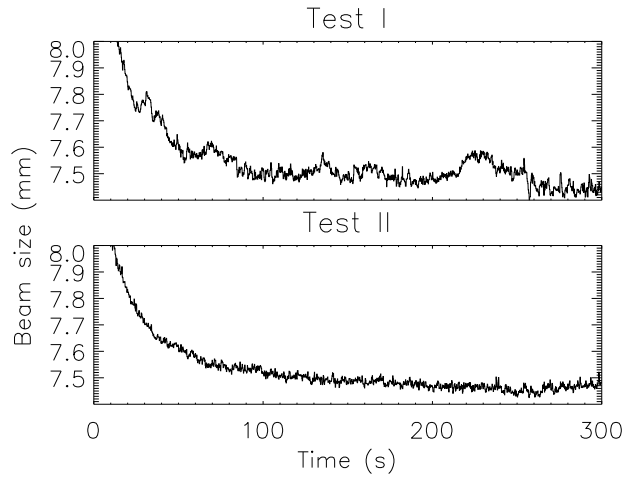

Fig. 3. Time dependence of the cavity mode size at the ETM, as recorded by the beam profiler, for relatively unstable mode-matching (Test I) and relatively stable mode-matching (Test II).

Wavefront gradient fields measured during Test I are shown in Fig. 4 (a) and (c). The corresponding off-axis wavefront distortions are shown in Fig. 4 (b) and (d). The wavefront distortion due to the absorption in the ITM and CP is largely distinct, as expected, with the right-hand and left-hand peaks being due to the ITM and CP respectively. The difference in the rates at which the distortions develop is also clearly evident.

4. Analysis of off-axis measurements

The measurements reported in the previous section show that the HWS is very sensitive and could be used to investigate the time-evolution of the distortion. The accuracy of the measured wavefront distortion will be confirmed in two independent ways. First, the measured distortion is analyzed to yield the on-axis defocus due to the absorption in the ITM and CP and this is compared to the defocus predicted by a finite-element model of the thermal lenses assuming the measured intra-cavity power. We then calculate the effect of the measured on-axis defocus on the cavity eigenmode and compare this to the mode size measured by the beam profiler. The procedure used for these calculations is described in this section and the results are presented in section 5.

4.A. Calculation of on-axis distortion

The expected off-axis wavefront distortion was calculated using the equations derived by Hello-Vinet [12], and using the parameters in Table 1, a 10 degrees off-axis angle and an ITM/CP separation on 140 mm, as shown in shown in Fig. 5 (a). The predicted distortion is shown in Fig. 5 (b), where the dashed lines indicate the distortion measured by Hartmann rays $A^{(off)}$ and $B^{(off)}$ that propagate in the vertical planes passing through the centres of the ITM and CP, as shown in Fig. 5 (a). Note that the peaks in the off-axis wavefront map do not occur exactly at the centres of the ITM and CP, as each ray samples the distortion due to both optics. Nevertheless, the distortion along these cross-sections, plotted in Fig. 6, has the largest defocus and these planes can thus be identified. Additionally, the simulation shows that the off-axis wavefront distortion for the cross-sections $A^{(off)}(y)$ and $B^{(off)}(y)$ can be calculated, to first order, using a linear sum of the on-axis distortions:

$$\begin{pmatrix} A^{(off)}(y) \\ B^{(off)}(y) \end{pmatrix} = \begin{pmatrix} 1 - \epsilon_1(t) & \delta_1(t) \\ \delta_2(t) & 1 - \epsilon_2(t) \end{pmatrix} \cdot \begin{pmatrix} A^{(on)}(y) \\ B^{(on)}(y) \end{pmatrix} \tag{2}$$

where $A^{(on)}(y)$ and $B^{(on)}(y)$ are the on-axis distortions due to each of the ITM and CP, shown in Fig. 5 (a). The parameters $\epsilon_1(t)$ and $\epsilon_2(t)$ are perturbations due to horizontal elongation or smearing of the thermal lenses. The parameters $\delta_1(t)$ and $\delta_2(t)$ are perturbations representing the cross-contamination of the wings of one distortion into the center

7

(a) $t_{\mathrm{expt}} = 7.06$s

(b) $t_{\mathrm{expt}} = 7.06$s

(c) $t_{\mathrm{expt}} = 291.39$s
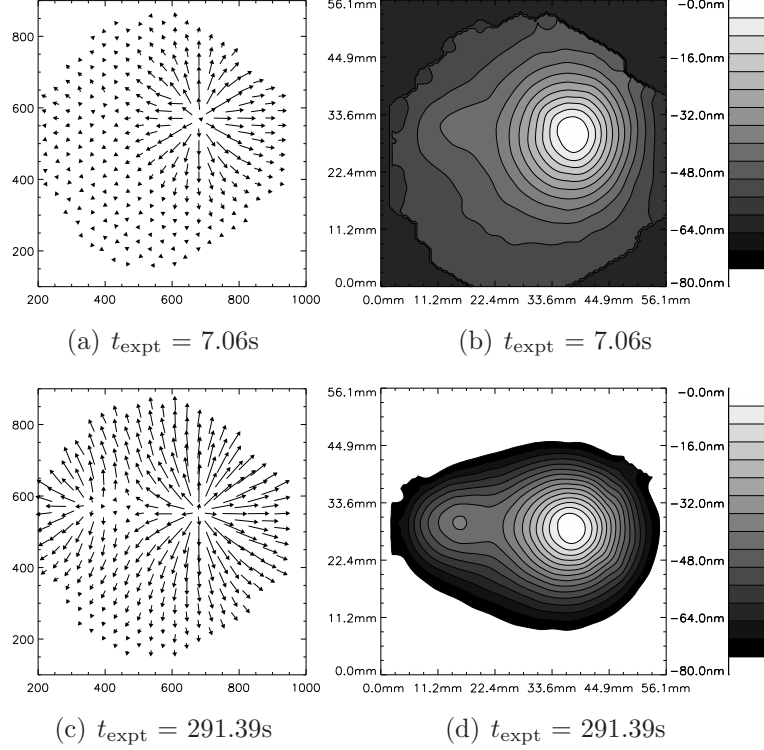
(d) $t_{\mathrm{expt}} = 291.39$s

Fig. 4. Wavefront distortion gradient fields and off-axis maps at two times after storing power in the Fabry-Perot cavity. (a) and (c) show the gradient fields, calculated by dividing the absorption-induced transverse displacement of the centroids by the HWS lever arm distance. The magnitude of the gradient at each point is proportional to the length of the vector. The HWS only measures the gradient of the wavefront. Hence we set the zero value of the wavefront distortion to be at the center of the RH lobe. Note that the wavefront distortion in (d) has saturated the lower end of the scale. The numbers on the axes indicate the coordinates on the HWS CCD in pixels; 1 pixel corresponds to about 72 μm at the ITM. (b) and (d) were calculated by numerically integrating the displacement fields [16, 22].
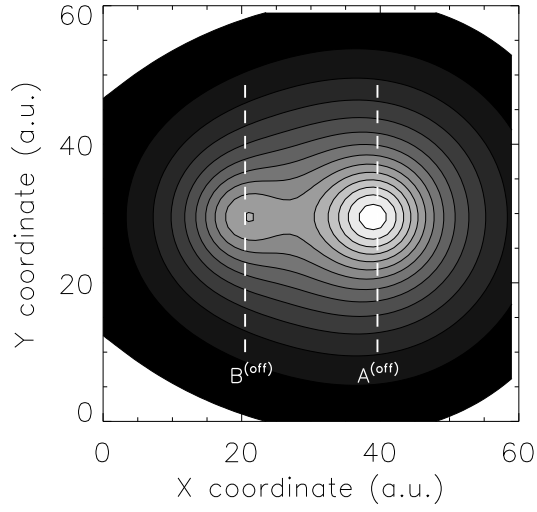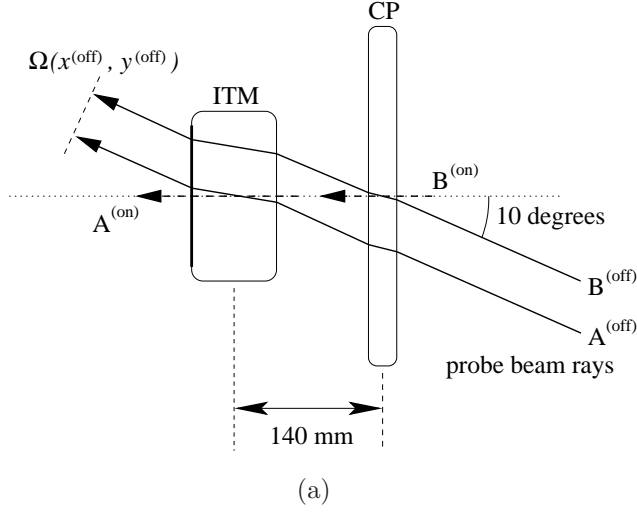
(a)

(b)

Fig. 5. (a) Off-axis probe beam refracting through sapphire ITM and fused silica CP. The rays $A^{(off)}(y)$ and $B^{(off)}(y)$ pass through the centres of the ITM and CP, respectively. $A^{(on)}(y)$ and $B^{(on)}(y)$ are the corresponding on-axis versions of these rays. (b) Predicted off-axis wavefront distortion showing the two vertical cross-sections, $A^{(off)}$ and $B^{(off)}$, used to determine the defocus in the sapphire and fused-silica, respectively.
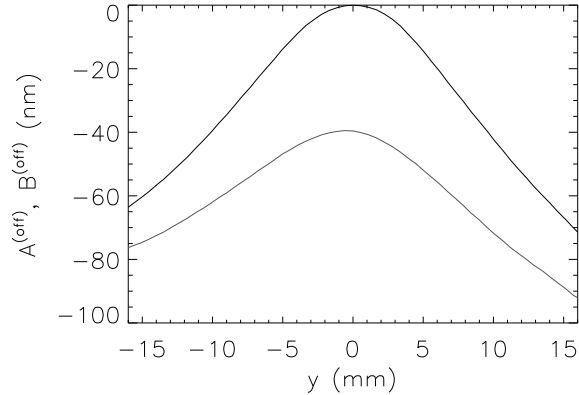
Fig. 6. Vertical cross-sections of wavefront distortions $A^{(\text{off})}$ (upper) and $B^{(\text{off})}$ (lower) from Test I at time $t = 291.39\,\text{s}$

of the other. The parameters $\epsilon_1(t)$, $\epsilon_2(t)$ and $\delta_2(t)$ quickly reach their equilibrium values of 0.032, 0.008 and 0.056 respectively. The coefficient $\delta_1(t)$, however, develops more slowly, due to the poor thermal conductivity of fused silica and at t = 300 s the coefficient $\delta_1(t)$ is approximately 0.040 [23].

Since both the distortion in the CP and the δ_1 perturbation are small, its long time constant will not significantly affect the time-evolution of the off-axis distortion. Thus, the on-axis wavefront distortion is calculated by inverting the matrix in Eqn. 2:

$$
\begin{pmatrix} A^{(\text{on})}(y) \\ B^{(\text{on})}(y) \end{pmatrix} \approx \begin{pmatrix} 1 + \epsilon_1(t) & -\delta_1(t) \\ -\delta_2(t) & 1 + \epsilon_2(t) \end{pmatrix} \cdot \begin{pmatrix} A^{(\text{off})}(y) \\ B^{(\text{off})}(y) \end{pmatrix} \tag{3}
$$

4.B. Defocus of the cavity mode

A schematic diagram showing the Hartmann beam and the cavity mode interacting with the volumetric (thermo-optic and elasto-optic) and surface (thermo-elastic) lenses is illustrated in Fig. 7. The relative magnitudes of these effects in sapphire and fused silica have previously been determined [24] and are summarized in Table 2. The distortions acquired on transmission through the substrate are denoted v_1 and v_2 for fused silica and sapphire, respectively and the distortions acquired on transmission through the surfaces are denoted s_1 and s_2 for fused silica and s_3 and s_4 for sapphire.

With the exception of the surface deformation, s_4, the cavity mode experiences every volumetric distortion and surface deformation twice while the probe beam experiences them once. Additionally, the probe beam experiences the surface deformation s_4 on transmission
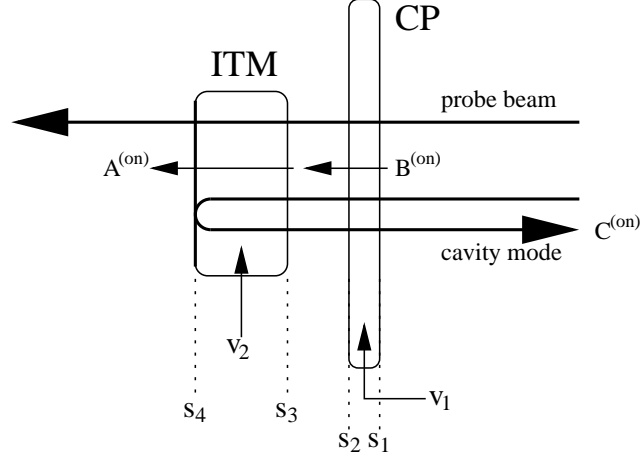
10

Fig. 7. The probe beam is transmitted through both the distorted substrates, v_1 and v_2, and through all deformed surfaces, s_1 to s_4. The cavity mode is transmitted through both the distorted substrates, v_1 and v_2, and through deformed surfaces, s_1 to s_3 and is reflected from the deformed surface s_4. The total wavefront distortion accumulated by the cavity mode is denoted $C^{(on)}$.

while the cavity experiences it on reflection. The distortion added to the cavity mode is therefore $2n_s/(n_s - 1)$ times larger than that added to the probe beam, where $n_s = 1.75$ is the refractive index of sapphire. The total wavefront distortion accumulated by the cavity mode, $C^{(on)}(y)$, is thus given by [23]:

$$C^{(on)}(y) \approx \frac{\frac{2\,n_s}{n_s-1}\,s_4 + 2\,(v_2 + s_3)}{v_2 + s_3 + s_4} A^{(on)}(y) + 2\,B^{(on)}(y) \tag{4}$$

$$\approx 2.53\,A^{(on)}(y) + 2\,B^{(on)}(y) \tag{5}$$

The defocus experienced by the TEM_{00} mode in the cavity due to $C^{(on)}(y)$, S_{TL}, is determined using the method of Arain et $al.$ [25] which calculates the maximum value of the overlap integral, $I(S)$, between the distortion and a spherically curved mirror. The overlap integral is given by

$$I(S) = \int_{-\infty}^{+\infty} \sqrt{\left(\frac{2}{\pi}\right)} \frac{1}{w_{\text{ITM}}} \exp\left(-y^2 \left[\frac{2}{w_{\text{ITM}}^2}\right]\right) \times$$
$$\exp\left(i\,\frac{4\,\pi}{\lambda} \left[C^{(on)}(y) - S\,y^2\right]\right) dy \tag{6}$$

where w_{ITM} is the cavity mode size at the ITM. The defocus due to the thermal lenses, S_{TL}, is the value of S that maximizes the magnitude of the integral. Since w_{ITM} depends on S_{TL},

11

	Sapphire	Fused Silica
Thermooptic Effect	1	1
Elastooptic Effect	0.2	-0.01
Thermoelastic expansion	0.8	0.06
Volumetric distortion	$v_2 = 1.2$	$v_1 = 0.99$
Surface deformation	$s_4 = s_3 = 0.4$	$s_2 = s_1 = 0.03$

Table 2. Sizes of the thermooptic effect, thermoelastic deformation, the elastooptic effect, the volumetric distortion on transmission and the surface deformation on transmission relative to the size of the thermooptic effect. v_1, v_2 and s_1, ..., s_4, refer to the types and locations at which these effects occur as indicated in Fig. 7. Note that the distortion through a single surface of the optic is simply half of the value of the thermo-elastic expansion.

this integral must be iterated several times, each time updating the value of w_{ITM}, until S_{TL} converges to a solution.

The cavity eigenmode size is then found using the cavity g-parameters [26]:

$$g_{ETM} = 1 - \frac{L_{cav}}{R_{ETM}}, \quad g_{ITM}(S_{TL}) = 1 - S_{TL} L_{cav},$$

where R_{ETM}, R_{ITM} are the radii of curvature of the end test mass and input test mass, respectively, and L_{cav} is the length of the cavity. The cavity mode size at the ETM, $w_{ETM}(S_{TL})$, is then given by

$$w_{ETM}(S_{TL}) = \sqrt{\frac{L_{cav}\,\lambda}{\pi}} \sqrt{\frac{g_{ITM}(S_{TL})}{g_{ETM}\left[1 - g_{ITM}(S_{TL})\, g_{ETM}\right]}}. \tag{7}$$

5. Results

5.A. Comparison of measured and predicted on-axis defocus

The temporal development of the defocus in the sapphire ITM and the fused silica CP was modelled using a finite element simulation. In the simulation the laser beam power transmitted through these optics was assumed proportional to the power measured by the BP, as shown in Fig. 2 (upper), with a beam size consistent with that measured at the ETM, as shown in Fig. 3 (upper). The average predicted defocus between t = 100s and t = 300s was normalised to that measured by the HWS.

The measured and predicted defocii are plotted as a function of time in Fig. 8. The difference between the two curves is also plotted using the right hand scale in Fig. 8, and
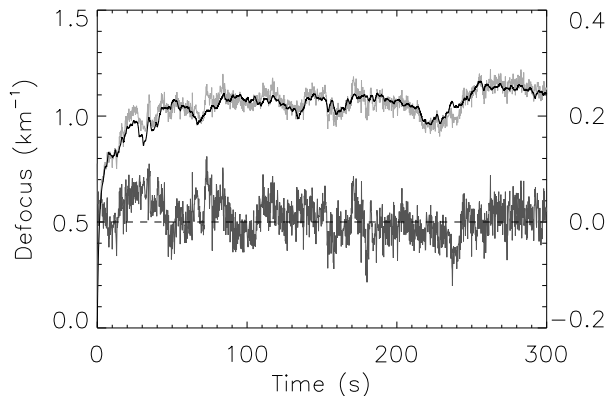
Fig. 8. A comparison of the defocus predicted by the finite element model (black curve) and the defocus measured by the HWS (light grey curve). The difference between the two (lower curve) is plotted using the right hand scale; it has an rms value of approximately $0.03\,\mathrm{km^{-1}}$.

has an rms value of approximately $0.03\,\mathrm{km^{-1}}$. There is clearly good agreement between the finite element model of the defocus and the defocus measured by the HWS sensor for the duration of the 300 s test. Note that the prediction appears to have less bandwidth than the measurement because of the slow thermal responses of the ITM and CP to power fluctuations.

5.B.   *Correlation of measured distortion and cavity mode size*

The cavity mode size at the ETM, as measured by the beam profiler during Test I, and the mode size calculated using the HWS were also compared (with no scaling or fitting parameters applied). The results are plotted in Fig. 9. There is excellent agreement between the overall magnitude of the predicted mode size using the HWS result (light grey) and the measured cavity mode size (black). There is also a clear correlation between the temporal fluctuations in the measured and predicted mode sizes. The difference between the measured and predicted cavity mode sizes is also plotted in Fig. 9, using the right hand scale, and has an rms value of approximately 0.05 mm.

The cavity was unlocked shortly after $t = 300\,\mathrm{s}$. As there is then no power in the cavity mode, there is no data from the BP after this time. The HWS, however, continued to observe the thermal lenses in the intra-cavity optics and the decay of these lenses is evident in Fig. 9, which shows the mode size at the ETM returning to the cold-cavity size in an exponential fashion.
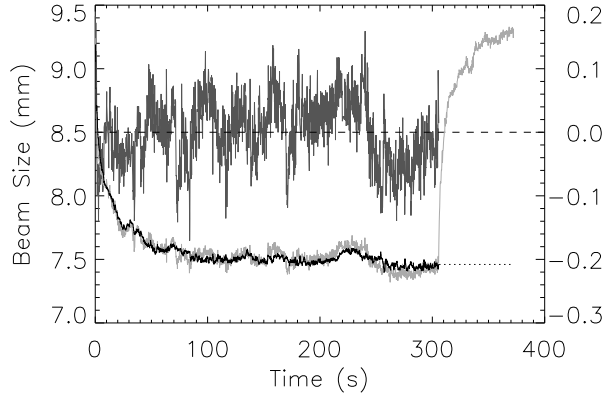
13

Fig. 9. Comparison of the beam size measured using the BP (black curve) and the beam size calculated using the HWS (grey curve). The difference between the two (upper curve) is plotted using the right hand scale; it has an rms value of approximately 0.05 mm. At t = 310s the cavity is unlocked and the HWS beam size returns to the cold-cavity value as the thermal lenses decay.

6. Conclusion

The results described here demonstrate the feasibility of using a HWS in-situ to measure absorption-induced wavefront distortion in optics that are suspended in a large vacuum system. The sensitivity of the sensor was $\lambda/730$ where $\lambda = 800$ nm (averaged over 10 frames), which was less than the fundamental or shot-noise limited sensitivity, probably due to residual air currents. The HWS was validated by showing that the measured distortion, when analyzed and converted to defocus, was consistent with the defocus predictions of a FEM of the ITM and CP assuming the measured cavity power, with an rms error of approximately $0.03\,\mathrm{km}^{-1}$. Additionally, we showed that the cavity mode size predicted using the measured distortion agreed to within 0.05 mm (rms), about 0.7%, with the measured mode size.

These results thus indicate that the installed HWS is both sufficiently sensitive for the measurements of absorption-induced wavefront distortion in advanced GWI and is accurate. Importantly, the HWS provides a direct and detailed measurement of the variation of the wavefront distortion, rather than a measurement that relies on the validity of assumptions and models. Although the wavefront distortion was characterized by the defocus in this instance, the wavefront profile is rich in spatial information that is necessary for any future multi-dimensional compensation systems, allowing for more effective compensation of thermal effects.

14

Acknowledgements

References

1. D. S. (for the LIGO Science Collaboration), "Status of the LIGO detectors," Classical Quant. Grav. **23**, S51–S56 (2006).

2. F. Acernese *et. al.*, "The status of VIRGO," Classical Quant. Grav. **23**, S62–S70 (2006).

3. H. Lück *et. al.*, "The GEO 600 gravitational wave detector," Classical Quant. Grav. **23**, S71–S78 (2006).

4. M. Ando and the TAMA Collaboration, "Current status of TAMA," Classical Quant. Grav. **19**, 1409–1419 (2002).

5. S. J. Waldman (for the LIGO Science Collaboration), "Status of LIGO at the start of the fifth science run," Classical Quant. Grav. **23**, S653–S660 (2006).

6. B. Abbott *et. al.*, "Upper limits on a stochastic background of gravitational waves," Phys. Rev. Lett. **95**, 221101–1 – 221101–6 (2005).

7. B. Abbott *et. al.*, "Search for gravitational-wave bursts in LIGO data from the fourth science run," Classical Quant. Grav. **24**, 5343–5369 (2007).

8. B. Abbott *et. al.*, "Analysis of LIGO data for gravitational waves from binary neutron stars," Phys. Rev. D **69**, 122001–1 – 122001–16 (2004).

9. B. Abbott *et. al.*, "Limits on gravitational-wave emission from selected pulsars using LIGO data," Phys. Rev. Lett. **94**, 181103–1 – 181103–6 (2005).

10. A. Weinstein, "Advanced LIGO optical configuration and prototyping effort," Classical Quant. Grav. **19**, 1575–1584 (2002).

11. K. Kuroda and the LCGT Collaboration, "The status of LCGT," Classical Quant. Grav. **23**, S215–S221 (2006).

12. P. Hello and J.-Y. Vinet, "Analytical models of thermal aberrations in massive mirrors heated by high power laser beams," J. Phys.-Paris **51**, 1267–1282 (1990).

13. P. Hello and J.-Y. Vinet, "Analytical models of transient thermoelastic deformations of mirrors heated by high power CW laser beams," J. Phys.-Paris **51**, 2243–2261 (1990).

14. R. Lawrence, D. Ottaway, M. Zucker, and P. Fritschel, "Active correction of thermal lensing through external radiative thermal actuation," Opt. Lett. **29**, 2635–2637 (2004).

15. M. Smith and P. Willems, "Auxiliary optics support system conceptual design document, vol. 1: Thermal compensation system," Technical Note T060083-00, LIGO (2006). http://www.ligo.caltech.edu/docs/T/T060083-00/T060083-00.pdf.

16. A. F. Brooks, T.-L. Kelly, P. J. Veitch, and J. Munch, "Ultra-sensitive wavefront measurement using a Hartmann sensor," Opt. Express **15** (2007).

17. P. Barriga *et al.*, "Technology developments for ACIGA high power test facility for advanced interferometry," Classical Quant. Grav. **22**, S199–S208 (2005).

18. C. Zhao, J. Degallaix, L. Ju, Y. Fan, D. G. Blair, B. J. J. Slagmolen, M. B. Gray, C. M. Lowry, D. E. McClelland, D. J. Hosken, D. Mudge, A. Brooks, J. Munch, P. J. Veitch, M. A. Barton, and G. Billingsley, "Compensation of strong thermal lensing in high-optical-power cavities," Phys. Rev. Lett. **96**, 231101–1 – 231101–4 (2006).

19. J. Degallaix, "Compensation of strong thermal lensing in advanced interferometric gravitational waves detectors," Ph.D. thesis, The University of Western Australia (2006).

20. D. Hosken, D. Mudge, C. Hollitt, K. Takeno, P. Veitch, M. Hamilton, and J. Munch, "Development of power scalable lasers for gravitational wave interferometry," in "Tokyo-Adelaide Joint Workshop Quarks, Astrophysics and Space Physics Tokyo, Japan, 6-10 Jan. 2003," (2003), no. 151 in Prog. Theor. Phys. Supp., pp. 216–220.

21. Z. Jiang, S. Gong, and Y. Dai, "Monte-Carlo analysis of centroid detected accuracy for wavefront sensor," Opt. Laser Technol. **37**, 541–546 (2005).

22. W. H. Southwell, "Wave-front estimation from wave-front slope measurements," J. Opt. Soc. Am. **70**, 998 – 1006 (1980).

23. A. F. Brooks, "Hartmann wavefront sensors for advanced gravitational wave interferometers," Ph.D. thesis, The University of Adelaide (2007).

24. R. Lawrence, "Active wavefront correction in laser interferometric gravitational wave detectors," Ph.D. thesis, Massachusetts Institute of Technology (2003).

25. M. Arain, G. Mueller, D. Reitze, and D. Tanner, "A note on optimal spherical approximation to thermal lensing," Technical Note LIGO-T060080-00-Z, LIGO (2006). http://www.ligo.caltech.edu/docs/T/T060080-00.pdf.

26. A. E. Siegman, *Lasers* (University Science Books, 1986).